Computers and Chemical Engineering 143 (2020) 107069

Contents lists available at ScienceDirect

Computers and Chemical Engineering

journal homepage: www.elsevier.com/locate/compchemeng

Computational fluid dynamics-based in-situ sensor analytics of direct metal laser solidification process using machine learning

Yi Ming Ren[a], Yichi Zhang[a], Yangyao Ding[a], Yongjian Wang[a,b], Panagiotis D. Christofides[a,c,*]

[a] Department of Chemical and Biomolecular Engineering, University of California, Los Angeles, CA, 90095-1592, USA
[b] College of Information Science and Technology, Beijing University of Chemical Technology, Beijing, 100029, China
[c] Department of Electrical and Computer Engineering, University of California, Los Angeles, CA 90095-1592, USA

ARTICLE INFO

Article history:
Received 23 July 2020
Revised 17 August 2020
Accepted 18 August 2020
Available online 20 August 2020

Keywords:
Additive manufacturing
Direct metal laser solidification
Computational fluid dynamics
Sensor analytics
Convolutional neural networks
Deep learning

ABSTRACT

Direct metal laser solidification (DMLS) has been receiving increasing research interest in the additive manufacturing (AM) industry due to its outstanding performance in producing parts with ultra-high precision and variable geometries. However, the lack of appropriate in-situ disturbance detection techniques specialized for DMLS makes real-time quality control extremely difficult. In this work, a first-principles-based finite element method (FEM) model focusing on the heat transfer behavior of the DMLS process is developed. The model-produced thermal data is processed to reproduce the outputs of two industrially used sensors: the optical tomography (OT) sensor and the melt pool monitoring (MPM) sensor. In-situ sensor data analytics is then performed through the use of a convolutional neural network (CNN) to automatically detect disturbances from each sensor data during the build process in real-time. Transfer learning is applied to the pre-trained AlexNet backbone to efficiently construct the disturbance detection CNNs for each sensor, and overall accuracy of 73.4% and 82.8% is observed for the melt pool and the OT CNN, respectively. To further increase the accuracy, a cross-validation scheme is proposed to combine the results from both CNNs based on their confidence levels. The final results demonstrate that the testing accuracy increases to 90.4% when cross-validation between both sensor data analytics is applied. The developed machine-learning-based algorithms provides a methodology to perform real-time process data analytics and thereby reducing defect formation and increasing production throughput.

1. Introduction

Additive manufacturing (AM) was invented in the 1990s and it has been exploited for the manufacturing of industrial parts using various kinds of materials including polylactic acid (PLA) plastic, photopolymer, gypsum, metal alloys, etc. (Gibson et al., 2014). In the past 20 years, the market share has grown by 20 percent each year, which created massive opportunities in this field. In 2019, the AM industry reached around 10 billion dollars and was still evolving rapidly. Compared to conventional fabrication techniques in the industry such as casting, AM technologies are significantly more advantageous due to their rapid prototyping time, fast manufacturing speed, reduced production cost, and versatile build geometry (Nandwana et al., 2016). The adoption of AM techniques also demonstrates huge economic benefits, where a cost reduction of about 40% can be achieved (Baumers et al., 2017). Among the wide range of materials that can be manufactured with AM methods, metal alloys have particularly drawn attention in the academia and the industry, and have taken up to 30% of the total AM market, due to their use in high mechanical strength applications, such as tooling (Costa et al., 2005), pharmaceutical devices, and automotive equipment (Leal et al., 2017). Two major metal deposition methods are typically used in the industry: Directed Energy Deposition (DED) and Laser Powder Bed Fusion (LPBF) (Frazier, 2014). DED involves the melting of a powder or wire feed with an energy source to directly deposit a fused layer onto the substrate. It has the advantages of high printing speed and low-cost feedstock, but also faces low-resolution issues, causing significant part deformation and limited geometric capability. Thus, LPBF becomes the more suitable option for applications with complicated design, stringent yield strength, and high precision requirements, which are often encountered in the medical (Singh and Ramakrishna, 2017) and aerospace (Liu et al., 2017) industry.

* Corresponding author at: Department of Chemical and Biomolecular Engineering, University of California, Los Angeles, CA, 90095-1592, USA.
E-mail address: pdc@seas.ucla.edu (P.D. Christofides).

https://doi.org/10.1016/j.compchemeng.2020.107069
0098-1354/

In this paper, we focus on a subcategory of LPBF called the direct metal laser solidification (DMLS), which involves a laser power source with enough energy to fully melt each metal powder layer. To construct the desirable structure, the first step is to design the build geometry and support structure, if necessary, with computer-aided design (CAD) software. Based on the 3D (three-dimensional) CAD geometry, a specific AM operating recipe is developed, including the layer-by-layer laser scanning plan and the layer thickness. Before each layer is printed, appropriate space in the deposition chamber is first created in the build platform by lowering the platform base by exactly one layer thickness. Next, the recoater blade pushes the metal powder from the fresh powder stock onto the build platform to prepare a uniform powder bed. Then, according to the predefined recipe, the laser power source scans across the layer to melt the powder, and the molten powder subsequently resolidifies to form the desired solid part. Despite the demand for high resolution, many part failures are encountered in industrial manufacturing given errors and disturbances during the DLMS process. For example, unexpected laser variations including the defocusing of the laser beam or incorrect laser pulsing may lead to the formation of cold and hot zones on the powder bed. The thermal and mechanical stresses of the build part are highly dependent on the temperature, which is influenced by the laser power, the energy dissipation of the material phase change, and the conduction and convection within the deposition chamber. Thus, laser and cooling abnormalities may cause mechanical problems of the build part such as lack of fusion or keyholing (Grünberger and Domröse, 2014). In addition, recoater streaking and jamming can happen due to the undesired part deformation above the expected build surface (Gong et al., 2014). Although it is desirable to understand and control the disturbances, the relationship between the variety of potential disturbances and operating parameters (e.g., scanning strategy, laser power, hatch spacing, and scanning speed) is very difficult to generalize for different materials and build geometries (Delgado et al., 2012).

To better understand the physics in DMLS processes, several experimental works have utilized first-principles-based modeling and analysis methods for deterministic analyses. Arısoy et al. (2019) utilized a multi-physics algorithm of heat transport and mechanical strength analytics to understand the influence of melt pool on the mechanical property of microstructure. Yan et al. (2018) constructed an integrated model of the energy density, the material microstructure formation, and the resulting parts' mechanical responses. Also, other simulation models investigated the effect of operating parameters and strategies aided by FEM models. For example, Ramos et al. (2019) looked at different scanning strategies, and Dong et al. (2019) delved into the influence of hatch spacing on melt pool dimensions and associated part quality. In addition, experimental studies endeavored to optimize the part design based on model-predicted properties. For instance, Peralta et al. (2016) developed the approach of probabilistic rapid qualification design and utilized model-predicted results to reduce the overall qualification process time. Khurana et al. (2018) used the model-predicted thermal profile and stress analysis to formulate and optimize the design of build geometry and support structure.

Nevertheless, existing simulation models fail to reflect the laser heating induced damage to the part during the building process. Thus, to avoid this problem, in-situ sensor monitoring technologies are developed to record the manufacturing information. Many types of real-time monitoring technologies have been developed in the academia and the industry, including the physical powder bed images, the layer-wise temperature history maps, the melt pool dimension data, etc. Clijsters et al. (2014) developed an optical sensor setup that is connected with a field-programmable gate array (FPGA). This setup allows the transfer of sensor information at a sampling rate higher than 10 kHz. Everton et al. (2016) provided a general review of valuable sensors that can be integrated with all types of metal additive manufacturing methods and applications. Moreover, the EOS company has developed advanced monitoring devices which consist of EOSTATE Optical Tomography (OT), EOSTATE MELTPOOL, EOSTATE BASE, and EOSTATE POWDERBED (Scott, 2017). Due to the superior performance of EOS devices, they have been selected as the reference metrics in this work. However, several challenges are associated with the sensor data that make it difficult to be efficiently utilized. The two major issues that need to be addressed are the overwhelming data size and the data analytics efficiency to enable real-time process control. As demonstrated by EOS, high-resolution camera sensors provide pictures at a very fast sampling rate, which produces terabytes of data per build. It is impossible to accommodate all the information because of the limitations on the data transfer speed and storage space. In addition, it is also not possible for engineers to read and analyze sensor images manually. Thus, modern computational resources and the advanced data processing algorithms form a central component that ties the process information, data storage, and data analytics together. For example, Zhang et al. (2018) utilized the convolution matrix and support vector machine (SVM) techniques to extract and evaluate plume and spatter information. Scime and Beuth (2019) used scale-invariant feature transform (SIFT) to extract features from the images and then used histogram of oriented gradients (HOG) to relate melt pool abnormality with the resulting defects. The same group also tried using convolutional neural network (CNN) with transfer learning from an AlexNet backbone to classify physical disturbances like super-elevation and recoater jams. Yuan et al. (2019) exploited a semi-supervised learning algorithm, which bases the CNN model on the Temporal Ensemble method, to allow successful training with limited sensor images for bootstrap.

In this paper, we develop an automated data-flow that integrates the simulation model and a machine learning network for real-time process monitoring and sensor data analytics. The simulation models are tailored to incorporate possible disturbances, and sensor-specific outputs are generated from the simulation results to reflect realistic disturbances that might be identified in-situ during the manufacturing process. In particular, we first develop a model that simulates the heat transfer and phase change based on the operating parameter combination using COMSOL Multiphysics. Next, according to the EOSTATE OT and EOSTATE MELTPOOL measurements, the heat map sensor data are generated from the simulation model with disturbances introduced as classification categories. Then, two separate CNN networks are designed and trained with transfer learning with an AlexNet backbone to identify the problems that lie in the OT and Meltpool images, respectively. In addition, the two CNN results are cross-validated using meta-analysis to make a final robust decision. The accuracy of the trained CNN and the computation time are demonstrated to be applicable to the in-situ AM process monitoring purposes.

2. FEM model of DMLS and thermal sensor output

As discussed in the introduction, first-principles-based numerical simulations have been utilized to model the DMLS processes to understand the effects of the operating parameters on the final build part properties. In the presented work, we specifically tailor our simulation model to predict and reproduce in-situ sensor monitoring information produced during the real-time manufacturing process. In this section, we first discuss the construction of a time-dependent FEM model that integrates heat transfer, the phase changes between powder, liquid and resolidified metal, the associated boundaries, and the operating recipes. Next, the performance of the developed model is validated with respect to experimental

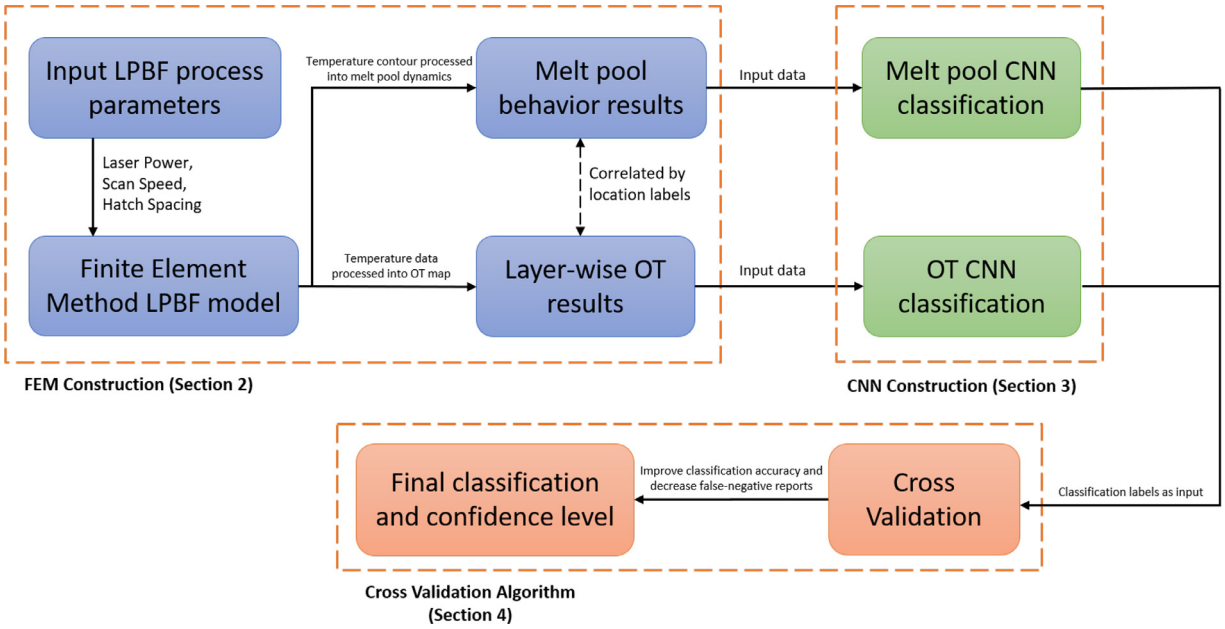

Fig. 1. Proposed automated data-flow which integrates FEM simulation and machine learning-based sensor data analytics.

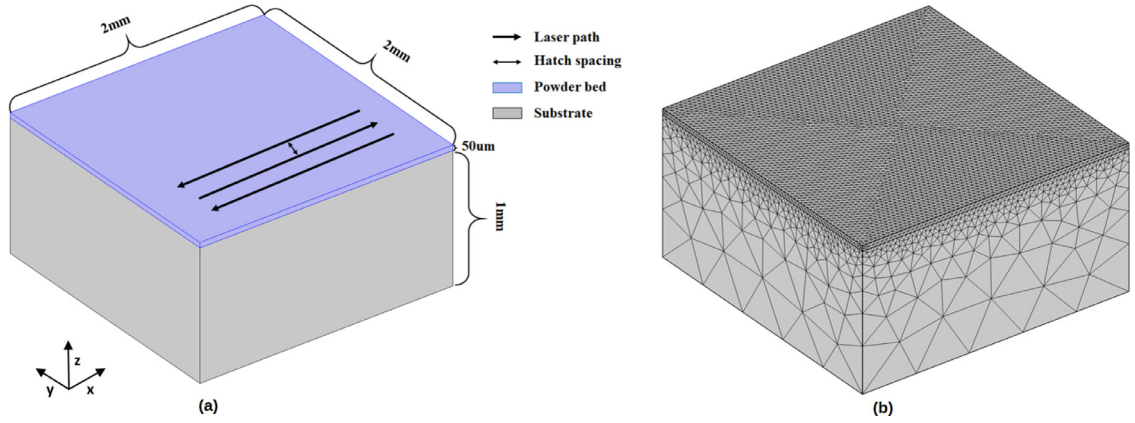

Fig. 2. (a) Build part geometry and scan pattern. (b) FEM mesh scheme. (For interpretation of the references to colour in this figure legend, the reader is referred to the web version of this article.)

data and theoretical standards. Then, we will discuss the details of the melt pool and thermal OT sensors and the procedures taken to process the simulation results to reproduce realistic sensor outputs.

2.1. Build part geometry and mesh

To ensure the generality of the developed method, a simple build geometry is adopted, which is a 1.4 × 1.5 mm rectangle with a height of 40 μm representing a single layer of IN-718 powder. The rectangular build part is printed on top of a square steel substrate with dimensions of 2.0 × 2.0 × 1.0 mm in length times width times height. This is shown in Fig. 2(a). The build part is positioned near the middle of the steel substrate so that there is sufficient room to the nearest boundaries to observe the heat transfer behavior.

As shown by the Fig. 2(b), the FEM model geometry is first meshed with two different mesh resolutions. Due to the powder layer being the domain where most heat transfer takes place, we generate a finer mesh for this domain with free tetrahedral mesh elements of a maximum element size of 3.32×10^{-5} m and a minimum element size of 2.16×10^{-6} m. Since we are mostly interested in the $x - y$ plane which is captured by the sensors, we employ a higher resolution factor for the x and y-directions than the z-direction. For the steel substrate mesh, we use a much lower resolution mesh to enhance computational efficiency. The z-axis is dynamically meshed so that the mesh nearest to the powder bed is much smaller in size than the one at the bottom. Such an inflation method gives rise to a maximum element size of 4.76×10^{-4} m and a minimum element size of 1.01×10^{-4} m.

2.2. Thermal energy transport governing equations

In this work, we utilize the heat transfer module from COMSOL Multiphysics to capture the major thermal characteristics of the DMLS process. In the proposed model, we consider the heat transport (conduction, convection, and radiation) and the associated boundary conditions, the latent heat of phase change, and the temperature/phase thermal dependent material properties. It is important to note that the model does not consider the detailed microstructure formation and the possible fluid flow within the melt pool. Fig. 3 summarizes the thermal boundary conditions

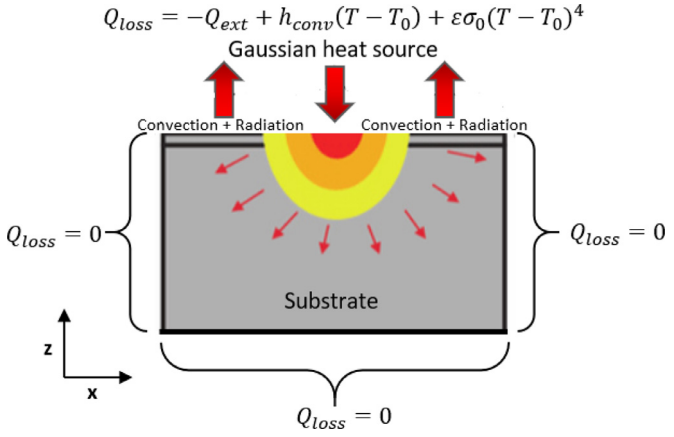

Fig. 3. Boundary conditions applied to the build part geometry. Gaussian heat source, convection, and radiation is considered for the top surface while no heat loss is assumed for the remaining surfaces.

used for FEM modeling in this study. The top powder surface considers the effect of the Gaussian laser source, convection, and radiation while the remaining surfaces assume no heat loss.

In each cell, the overall transient heat transfer is governed by the following heat balance equation:

$$\frac{\partial(\rho(T)C_p(T)T)}{\partial t} + \nabla q = q_s \tag{1}$$

where ρ is the density of the material, C_p is the specific heat capacity of the material, T is the temperature, and q_s is the rate of internal energy generation. Without the natural convection in the melt pool, the bulk energy transport is solely influenced by the conduction q as follows:

$$q = -\nabla(k(T)T) \tag{2}$$

where k is the thermal conductivity.

2.2.1. Boundary and initial conditions

The top surface boundary condition in the z-direction is described by the following equation:

$$-\frac{\partial(k(T)T)}{\partial z}(x, y, z = 0) = -Q_{ext} + h_c(T - T_0) + \epsilon\sigma_0(T^4 - T_0^4) \tag{3}$$

where h_c is the convective heat transfer coefficient, T_0 is the ambient gas temperature, ϵ is the emissivity, and σ_0 is the Stefan-Boltzmann constant. The heat loss due to convection and radiation is described by the second and the third term on the right hand side of the equation, respectively. In addition, the external heat source, Q_{ext}, is the laser source, which is assumed to have a Gaussian distribution:

$$Q_{ext}(r) = \frac{2AP}{\pi\omega^2} e^{-\frac{2r^2}{\omega^2}} \tag{4}$$

where A is the absorptivity, P is the laser power, ω is the laser beam radius, and r is the radial distance from the center of the laser beam.

For the other five surfaces, the assumption of no heat loss is assumed:

$$\frac{\partial(k(T)T)}{\partial x}(x = (0, l), y, z) = 0, \quad \frac{\partial(k(T)T)}{\partial y}(x, y = (0, w), z) = 0,$$
$$\frac{\partial(k(T)T)}{\partial z}(x, y, z = h) = 0 \tag{5}$$

where l is the length of the build platform, w is the width of the build platform, and h is the height of the build platform.

Table 1
IN-718 physical properties.

IN-718 properties	Value
solidus temperature	1533 K
liquidus Tempearture	1609 K
Latent heat of fusion	210 kJ/kg
Emissivity	0.35
Density, Specific heat, Thermal conductivity	See Fig. 4

In addition, the initial condition is that the temperature of the entire substrate at the beginning ($t = 0$) is at the ambient temperature of the printing chamber:

$$T(t = 0) = T_0 \tag{6}$$

2.2.2. Phase/temperature-dependent thermal properties

In our model, we consider three different phases of IN-718 alloy including powder, re-solidified metal, and liquid, which all have distinctive thermal properties. For metal alloys used in AM process such as IN-718, the melting point is not at a single temperature due to their mixed composition. Instead, a transitional zone of solid or liquid exists, which is defined by the solidus temperature and the liquidus temperature. Any material below the solidus temperature is considered to be purely in the solid phase, and similar logic applies for the liquidus temperature. While the solid and liquid phase of the material can be differentiated through the inspection of temperature, the powder and re-solidified metal phase of the material both exist in the same solid phase temperature range. In this model, we attempt to differentiate between the powder and re-solidified metal phase using porosity, ϕ, which is a function of local temperature:

$$\phi(T) = \begin{cases} \phi_0 & \text{if } T \le T_s \\ 0 & \text{if } T \ge T_l \\ \dfrac{\phi_0}{T_s - T_l}(T - T_l) & \text{if } T_s < T < T_l \end{cases} \tag{7}$$

where T_s is the solidus temperature, T_l is the liquidus temperature, and ϕ_0 is the initial porosity of the powder.

In addition, we are interested in the three temperature-dependent material properties that are important to the simulation: the specific heat capacity, the thermal conductivity, and the density of IN-718, whose profiles are shown in Fig. 4. Fig. 4 is plotted using experimental results reported from Romano et al. (2016). The heat capacity C_p is governed by functions of temperature at the solid and liquid phase, the latent heat of fusion l_f and the percentage at each phase θ also contribute to the effective heat capacity as follows:

$$C_p(T) = \begin{cases} C_{p,s}(T) & \text{if } T \le T_s \\ C_{p,l}(T) & \text{if } T \ge T_l \\ \dfrac{L_f}{T_l - T_s} + \theta_s C_{p,s}(T_s) + \theta_l C_{p,l}(T_l) & \text{if } T_s < T < T_l \end{cases} \tag{8}$$

where subscripts s and l refer to the solid and liquid phase, respectively. The key thermodynamic parameters are shown in Table 1. In contrast, the thermal conductivity and density of the powder and the re-solidified metal can be distinguished by porosity:

$$k_{powder} = k_{solid}(1 - \phi(T))^4 \tag{9}$$

$$\rho_{powder} = \rho_{solid}(1 - \phi(T)) \tag{10}$$

where k and ρ are the thermal conductivity and the density of the material, respectively. As stated in Eq. (7), ϕ is dependent on temperature, which makes k and ρ also indirectly dependent on temperature.

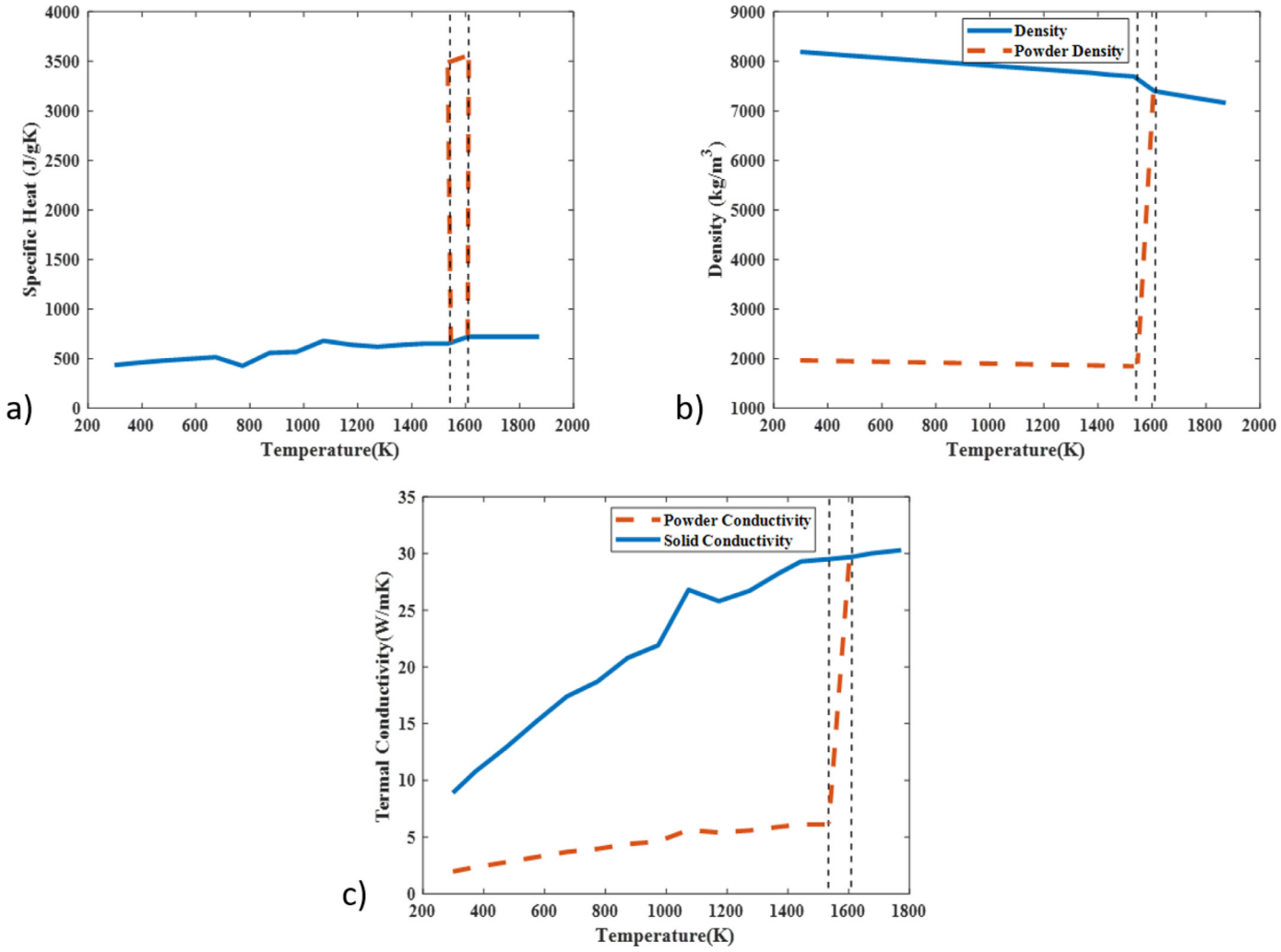

Fig. 4. Temperature dependent thermal properties of IN718: (a) specific heat capacity, (b) density, and (c) thermal conductivity. The vertical dotted lines represent the transition region between the solidus and liquidus temperature.

2.3. Model implementation and verification

To validate the model, a range of combinations of the laser power and the scan speed were tested. While laser power and scan speed influence the resulting melt pool differently, they are often used in conjunction to calculate the total laser energy density which dominates the comprehensive trend of the overall heating effect and melt pool dimensions. The energy density can be calculated as follows:

$$E = \frac{P}{V} \tag{11}$$

where E is the energy density, P is the laser power, and V is the scan speed.

Process parameters excluding laser power and scan speed are fixed at a constant 40 μm layer thickness and 0.1 mm hatch spacing. A commonly used bidirectional laser scanning scheme is chosen. In particular, the laser scans in the x-direction until reaching the build part's edge, jumps one hatch spacing in the y-direction, and then reverses the scanning direction along the negative x-direction. The range of operating conditions explored is listed in Table 2. The outputs collected from the FEM model are the melt pool dimensions and the temperature characteristics, which are compared to analytical solution to the Rosenthal equation and experimental findings.

Table 2
FEM model operating process parameters.

Process Parameters	Value
Laser power	70–300 W
Scanning speed	0.2-1.2 m/s
Hatch spacing	0.1 mm
Powder thickness	40 μm
Laser spot diameter	70 μm
Absorbance	0.6

2.3.1. Comparison with experimental results and solution to the rosenthal equation

First, we compare the melt pool dynamics developed in the FEM model with that of the experimental works (Sadowski et al., 2016), as shown in Table 3. It is demonstrated that the FEM model results closely resemble the experimental results for all operating combinations with an error smaller than 10%. One trend we observe is that the experimental values are constantly larger than the FEM results. The major reason behind this discrepancy between the FEM and experimental results can be attributed to the fact that the FEM model does not consider the influence of fluid flow of the molten metal in the melt pool. During the actual rapid heating process, the molten metal is driven outwards due to the higher

Table 3
Comparison between experimental and FEM model melt pool width.

Power (W)	Scan Speed (m/s)	Energy Density (J/m)	Experimental (μm)	FEM (μm)	Error
200	1.2	166.7	197.8–261.6	180.4	8.79%
200	0.7	285.7	184.9–300.9	173.2	6.33%
100	0.2	500.0	242.6–297.4	230.0	5.19%

Table 4
Ambient temperature (273 K) IN-718 thermal properties.

Thermal Property	Value
Absorptivity, λ	0.6
Density, ρ	8220 $kg \cdot m^{-3}$
Specific heat, C_p	43 $J(kg \cdot K)^{-1}$
Thermal conductivity, k	11.4 $W(m \cdot K)^{-1}$

surface tension in the outer sections of the melt pool compared to the inner sections of the melt pool (Ma et al., 2013). This phenomenon thus causes the experimental melt pool to be larger than the FEM model predicted melt pool.

In addition, the solution to the analytical Rosenthal equation is an important criterion that is often used to judge the melt pool dimension, which was originally developed for metal welding (Rosenthal, 1941). However, due to the similarity in the melting mechanism between welding and metal AM processes, the Rosenthal equation can be applied to describe the DMLS process. The following assumptions are made by the Rosenthal equation solution:

1. Thermophysical properties are temperature independent.
2. Quasi-stationary temperature distribution condition around melt pool.
3. Heat source is a point source.
4. Heat transfer is governed purely by conduction, ignoring convection and radiation.

Adopting these assumptions, the Rosenthal equation can be formulated as follows:

$$T = T_0 - \frac{\lambda P}{2\pi kr} exp\left(-\frac{V(r+\xi)}{2\alpha}\right) \tag{12}$$

where T_0 is the ambient temperature, λ is the absorptivity, P is the laser power, k is the thermal conductivity, V is the scanning speed, α is the thermal diffusivity, ξ is the x-direction moving coordinate expressed by $\xi = x - Vt$ as the laser moves along the x-axis, and r is the distance from the heat source defined as $\sqrt{\xi^2 + y^2 + z^2}$. The thermophysical properties of IN-718 for the above calculation are listed in Table 4.

Based on the Rosenthal equation, the width of the melt pool of low thermal diffusivity material including IN-718 can be estimated (Tang et al., 2017):

$$W \approx \sqrt{\frac{8}{\pi e} \frac{\lambda P}{\rho C_p V (T_m - T_0)}} \tag{13}$$

where W is the approximate melt pool width, T_m is the melting point of the material, and ρ is the density listed in Table 5. The differences between the analytical solution to the Rosenthal equation and the FEM generated melt pool dynamics and their respective errors are shown in Table 3. In general, the Rosenthal equation predicts the melt pool width to be larger than the FEM melt pool width. An explanation for this discrepancy is the assumptions made by the Rosenthal equation. As shown earlier, the Rosenthal equation assumes the thermophysical properties to be temperature independent, and only conductive heat transfer is considered. Due to the lack of consideration of convection and radiation heat loss, the solution to the Rosenthal equation estimates a larger melt pool width than the FEM model.

2.4. Sensor output representation

After the thermal performances are validated, we use our proposed FEM model to reproduce the industrial monitoring sensor output: the melt pool monitoring (MPM) sensor and the optical tomography (OT) sensor. The MPM sensor reports the detailed behavior of the region where the laser focuses on at each timestep. In contrast, the OT sensor outputs monitor the overall temperature map of the whole layer. These two sensors can provide different views and information about the thermal features of the build platform. As shown in the previous section, the FEM model is capable of producing realistic thermal results at any time interval, which demonstrates a great potential to reproduce the realistic MPM and OT intensity maps.

2.4.1. Melt pool

The MPM sensor aims to capture the melt pool behavior through the implementation of an on-axis photodiode sensor or a short-wave infrared (SWIR) camera that follows the laser scan pattern. It is capable of capturing high-quality melt pool dynamics due to its on-axis configuration and small focal domain. A typical melt pool photodiode sensor has a very high capturing rate in the range of 10 kHz to 25 kHz. Due to this high capture rate, the MPM sensor can generally produce near-continuous process monitoring. However, the disadvantages of the MPM sensor include its limited field of view, the influence from scanning parameters, and the huge amount of data to be generated, stored, and analyzed. It has been demonstrated in our previous section that the FEM model can directly reproduce the melt pool with reasonable dimensions. Starting with this preliminary result, we can reproduce the result of the MPM sensor through calibrating our camera sampling rate to that of a real sensor by tuning the FEM model solution sampling rate to 1×10^{-4} s, i.e., 10 kHz. Thus, the model generates near-continuous melt pool images similar to those produced by a realistic sensor. An example of a single melt pool captured by the FEM model is shown in Fig. 5.

2.4.2. Optical tomography (OT)

The OT sensor also tries to capture the thermal aspect of the DMLS process but it aims to generate a layer-wise temperature map of each build layer. The OT camera can usually be an infrared (IR) camera and has several different types including long-wave infrared (LWIR) or medium-wave infrared (MWIR). The OT sensor picks up the light intensity in a fixed sensor radius and processes these light signals into temperature values. Each temperature value is assigned to a region/pixel of the final image depending on the sensor specification. Under normal process operating conditions, the highest temperature values within the melt pool would contribute predominantly to the signal produced (Mohr et al., 2020). This is due to the nonlinearity of the temperature-intensity dependence relationship despite the rapid cooling of the material after the laser passes.

In order to reproduce the OT sensor results, we utilize the FEM model and the temperature information of individual mesh cells

Table 5
Comparison between experimental and FEM model melt pool width.

Power (W)	Scan Speed (m/s)	Energy Density (J/m)	Rosenthal Solution (μm)	FEM (μm)	Error
300	1.2	250.0	178.5	172.3	3.48%
200	0.7	285.7	190.8	173.2	9.23%
100	0.2	500.0	252.5	230.0	8.88%

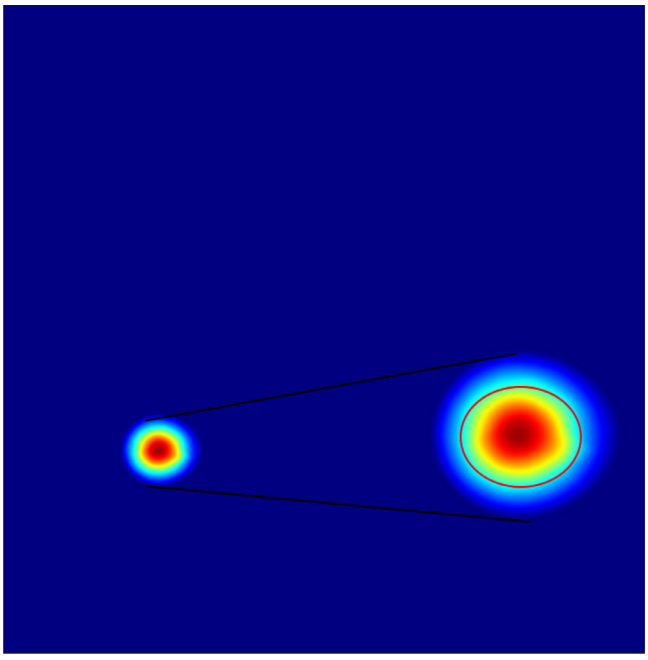

Fig. 5. Example melt pool image at one timestep generated by FEM. The melt pool region is zoomed in and is highlighted by the red circle. (For interpretation of the references to colour in this figure legend, the reader is referred to the web version of this article.)

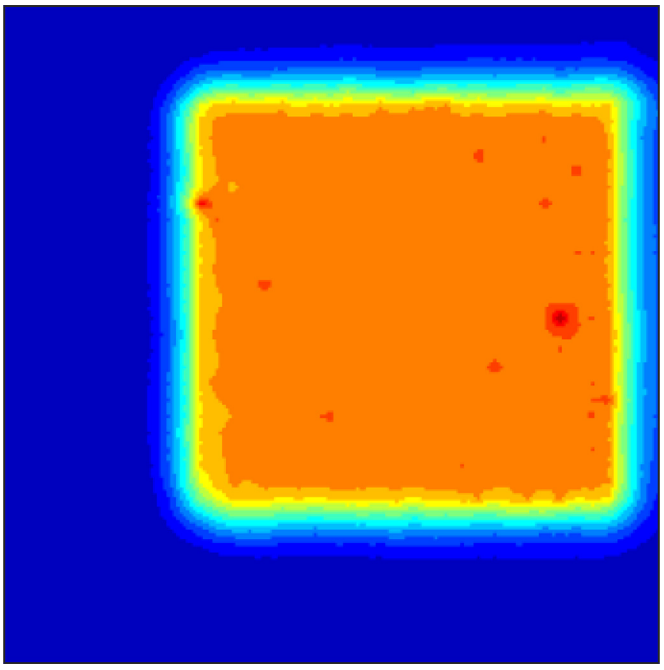

Fig. 6. Single layer temperature mapping processed to reproduce OT sensor output. The red spots represent the potentially overheated regions in various sizes due to process disturbances. (For interpretation of the references to colour in this figure legend, the reader is referred to the web version of this article.)

to create the layer-wise temperature map. Since the sensor radius is much larger than the individual FEM mesh cells, we average all of the values of mesh cells within the sensor radius and assign the averaged value as the final value for that sensor location at each capturing timestep. A sensor radius of 0.25 mm is used due to the build part's small dimensions. Then, we analyze the whole averaged temperature history of each previously defined radius and take the maximum temperature as the final value in our OT temperature map. An example of a single layer OT temperature map is shown in Fig. 6.

3. Sensor data analytics through convolutional neural network

After melt pool and OT sensor images are collected, in-situ data analyses need to be constructed for real-time analytics, as discussed in the introduction. In this work, we adopt the convolutional neural network (CNN), a deep learning technique that is widely adopted for image-processing. Through training, CNN is able to automatically detect the disturbances and defects in the build part during the manufacturing process with high accuracy and efficiency. In this section, first, we will discuss the construction of CNNs. Next, the prediction results from the trained constructed CNN trained for both melt pool data and OT data are discussed.

3.1. CNN construction

The major distinction of a convolutional neural network is the usage of convolutional layers to extract the correlational information from the high dimensional inputs, which makes CNN a good candidate for solving image recognition problems. A variety of trained general-purpose, high-performance CNN backbones, such as AlexNet, ResNet, and VggNet, have been demonstrated to produce highly-accurate image classifications. By changing only the final classification criteria and preserving the trained feature extraction functionality, CNN backbones can be easily modified and tailored to analyze DMLS sensor data. This process, which aims to specialize a pre-trained generic CNN model, is known as transfer learning (Goodfellow et al., 2016).

In this work, the AlexNet CNN backbone developed by Krizhevsky et al. (2012) is used as the base CNN architecture, and transfer learning is performed using MATLAB for the purpose of in-situ sensor data classification. Fig. 7 shows the data flow dimensions through the modified AlexNet CNN and Table 6 shows the specific dimensions of the proposed CNN. As shown in Fig. 7, the hidden layers consist of five sets of convolution layers followed by pooling layers and fully connected layers. The ReLU function, i.e., $ReLu(x) = \max(0, x)$, is applied between layers to introduce non-linearity, and Local Response Normalization (LRN) is performed to limit the unbounded output from the ReLu functions (Krizhevsky et al., 2012). In addition, dropout layers are implemented to reduce network overfitting and computational resources needed by randomly deactivating neurons. The CNN terminates with a softmax layer followed by a classification layer. During transfer learning, only the dense layers are restructured and retrained to identify features that are specific to the DMLS process using training data containing known errors in OT and MPM sensor data.

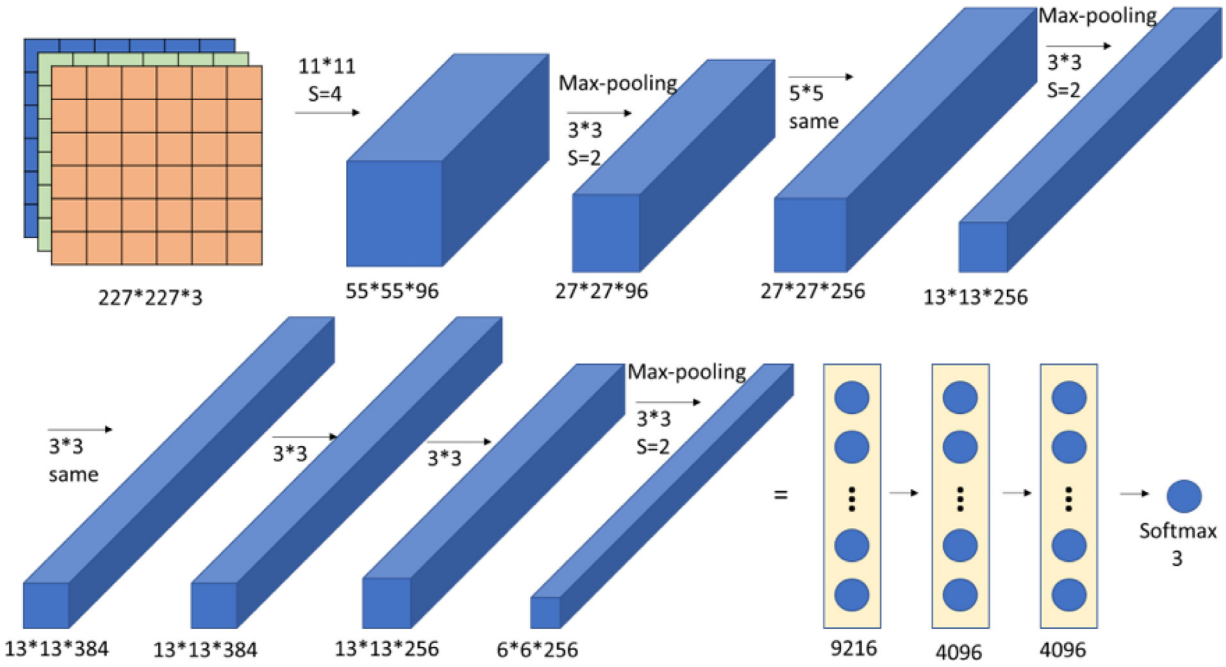

Fig. 7. Modified AlexNet convolutional neural network structure.

Table 6
Modified AlexNet convolutional neural network with specific layer dimensions.

Layer	Dimension	Number of filters
Input	227 × 227 × 3	
Convolution	11 × 11 × 3	96
ReLU		
Channel normalization (LRN)		
Max Pooling		
Convolution	5 × 5 × 96	256
ReLU		
Channel normalization		
Max Pooling		
Convolution	3 × 3 × 256	384
ReLU		
Convolution	3 × 3 × 384	384
ReLU		
Convolution	3 × 3 × 384	256
ReLU		
Max Pooling		
Fully Connected		
ReLU		
Dropout		
Fully Connected		
ReLU		
Dropout		
Fully Connected	1 × 1 × 4096	
Softmax		
Classification	3	

The exact structure and dimensions of the crucial layers are shown in Table 6. Specifically, the training data are the melt pool and the OT images generated from the FEM model and will be used to train their own respective CNN. The melt pool images are exported from the FEM model with a resolution of 227 × 227 pixels in order to match the AlexNet input requirement. However, since each OT image represents the entire build platform, a resolution of 227 × 227 pixels is too low to capture all information. Therefore, through trials-and-errors, each OT image is dissected into 20 × 20 sub-regions of size 227 × 227 pixels to preserve all information in the original image, and each regional OT image is individually processed by the CNN.

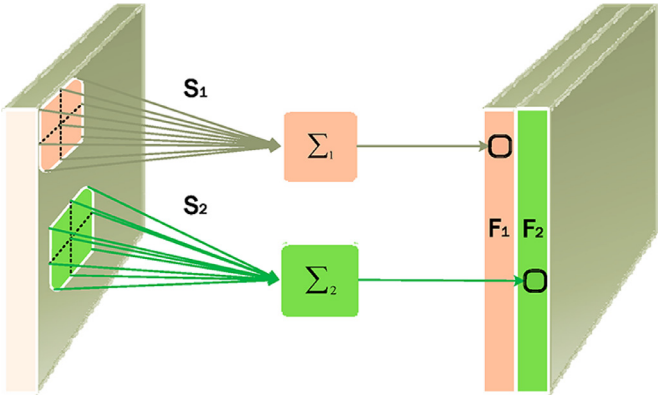

Fig. 8. Convolutional process of transforming the input image using filters S to feature maps F.

After passing the initial input layer, the processed input images enter sets of combinations of convolution layers and pooling layers. By using trained weighted matrices known as filters or kernels, the convolution layers are able to recognize specific features. A CNN may contain multiple sets of convolution layers to extract different levels of features. It has been demonstrated that early filter layers recognize primitive features such as lines, edges, or corners, whereas latter layers can distinguish more abstract parts of the desired object, such as heads of animals and wheels of cars. This hierarchy of abstractions allows the implementation of transfer learning as features of low-level abstraction are often consistent throughout all geometries. For example, in the AM process, operational disturbances are usually distinguished by distinctive edges or lines in the heat map. Thus, a well-trained filter can be easily applied to various processes. A successful implementation of transfer learning may only require the re-adaptation of high-level filters or even just the final classification layers.

When a region of the input image is transformed by the filter, S_i, it is converted to a region on the output feature map, F_i, which retains the feature extracted by the certain filter as shown in Fig. 8.

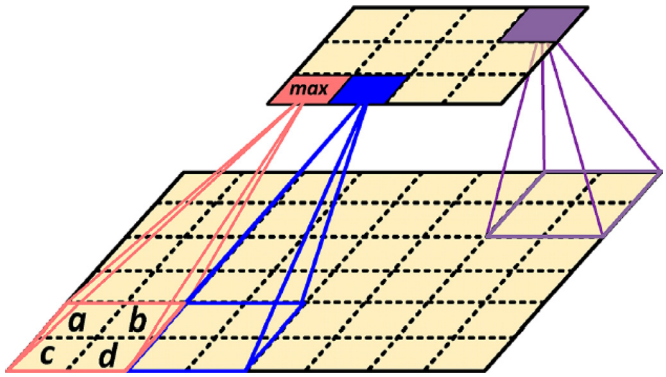

Fig. 9. Max pooling process of an input convoluted layer.

Following the convolution layers, which expand the overall dimensions of the input data through the creation of multiple feature maps for each filter, pooling is performed to down-sample and summarize the feature map results (Goodfellow et al., 2016). In this work, the max-pooling down-sampling method is used, as shown in Fig. 9. Max pooling extracts the maximum value from multiple pixels in a predefined region of the input layer, also known as the pooling window, and stores it in one pixel of the pooling layer. The process repeats as the pooling window slides across all of the input pixels, and the sliding distance is known as stride size. A 3×3 pooling window with a stride size of 2 is utilized in Alexnet.

After the convolutional layers and pooling layers have extracted features and reduced the overall dimensionality, fully connected layers are used to perform classification. Through training, each extracted feature from the convolutional layers is assigned weights with respect to each classification category. Then, the fully connected layers use the weight matrices to compute the confidence level of the input belonging to each category. In this work, the last fully connected layer has input dimensions of $1 \times 1 \times 4096$ pixels and it computes the confidence levels of the input images with respect to each of the three final categories. Finally, as shown in Fig. 10, the output of the fully connected layer undergoes the softmax function, i.e., $\sigma(\vec{z}) = \frac{e^{z_i}}{\sum_{i=1}^{k} e^{z_i}}$ for $\vec{z} \in \mathbb{R}^k$, where the most likely category will be chosen as the final classification result.

Stochastic gradient descent algorithm is used to train the neural network model through the alternation of model weights based on the computed gradients. Specifically, the input training data is first forward-propagated to calculate the loss function:

$$L = -\sum_{i=1}^{3} y_i \log(\hat{y}_i) \tag{14}$$

where L is the loss, y and $\hat{y}$ are the ground-truth label and predicted classification label, respectively. Given the loss function, the model weights are updated using the gradient computed from back-propagation (Amari, 1993). Following this approach, the CNN is trained for multiple epochs until the desired convergence criterion is reached. One training epoch corresponds to the entire training dataset being propagated through once. The changes made to the weights during each training epoch are affected by the learning rate which determines how quickly the model adapts to the problem.

3.2. Individual sensor data analytics through CNN

As mentioned in the previous section, both the melt pool and the OT CNNs share the same structure using the modified AlexNet backbone. The use of different sets of training images during transfer learning enables the melt pool CNN and OT CNN to recognize disturbances in melt pool images and OT images, respectively. In this section, we first discuss the selection details regarding each CNN's training and validation image sets. Next, we discuss the hardware used for training and the specific training options assigned for each CNN. Finally, we further test our CNNs and analyze the testing results of each CNN using the corresponding confusion matrix.

3.2.1. Melt pool and OT CNN training

Before either CNN is trained, training images must be labelled with ground truth, i.e., the categories that images actually belong to, and their respective locations on the build plate. Both types of sensor images are split into three categories: proper-melting, under-melting, and over-melting. A total of nine simulations are performed under various disturbances to collect melt pool and OT CNN training images. Disturbances are implemented by varying the laser power from 70.0 W to 437.5 W to create under-melting and over-melting regions. For the melt pool CNN, five simulation results are used for training where 1000 images are produced during each simulation. We notice that the melt pool image dataset contains much more proper-melting images than under-melting and over-melting images. Therefore, we carefully choose the proportion of images for each category and exclude excessive proper-melting images to ensure model accuracy by preventing class imbalance. The final melt pool CNN training dataset contains a total of 1412 different melt pool images, of which 710 correspond to proper-melting, 376 correspond to over-melting, and 326 correspond to under-melting. For OT CNN, all nine simulation results are used for training, where 400 regional OT images are produced during each simulation. Among these 400 regional OT images, 231 of them are images of the powder bed which the laser does not pass through and thus only 169 of them are images of interest. Similar to the melt pool CNN, regional OT images are selectively used for training to avoid class imbalance. The final training dataset for the OT CNN consists of 1173 regional images, in which 705 correspond to proper-melting, 274 correspond to over-melting, and 194 correspond to under-melting. Additionally, among the training image dataset for both CNNs, 70% of the images are randomly selected as training data while the rest 30% are used as validation data.

The OT CNN is trained for a total of 8 epochs with a learning rate of 2×10^{-4} as further training does not increase the CNN performance significantly. The total time to train the OT CNN is around 4 hours on a 6 GB Nvidia GeForce GTX 1060 GPU and the final training accuracy of the OT CNN is 86.2%. The melt pool CNN is trained for a total of 12 epochs. It is observed that the training of the melt pool CNN is more sensitive to the learning rate, which is likely to be due to the higher contrast in the melt pool images. Therefore, a lower learning rate of 1×10^{-5} is used. The total time to train the melt pool CNN is around 8 hours using the same GPU and the final training accuracy achieved is 89.3%.

3.2.2. Melt pool and OT CNN testing

In order to further test the accuracy and robustness of the trained CNNs, additional melt pool and OT images are collected and tested. The OT CNN test set consists of a total of 156 regional images, in which 86 correspond to proper-melting, 28 correspond to over-melting, and 42 correspond to under-melting. The melt pool CNN test set consists of a total of 678 melt pool images, in which 446 correspond to proper-melting, 135 correspond to over-melting, and 97 correspond to under-melting. The testing results of the two models are shown by the confusion matrices in Fig. 11. The confusion matrix is commonly used as the metric to demonstrate the accuracy of classification results, which has the dimensions of $\mathbb{R}^{(N+1)\times(N+1)}$, where N represents the number of categories involved in the classification. The categories are laid out

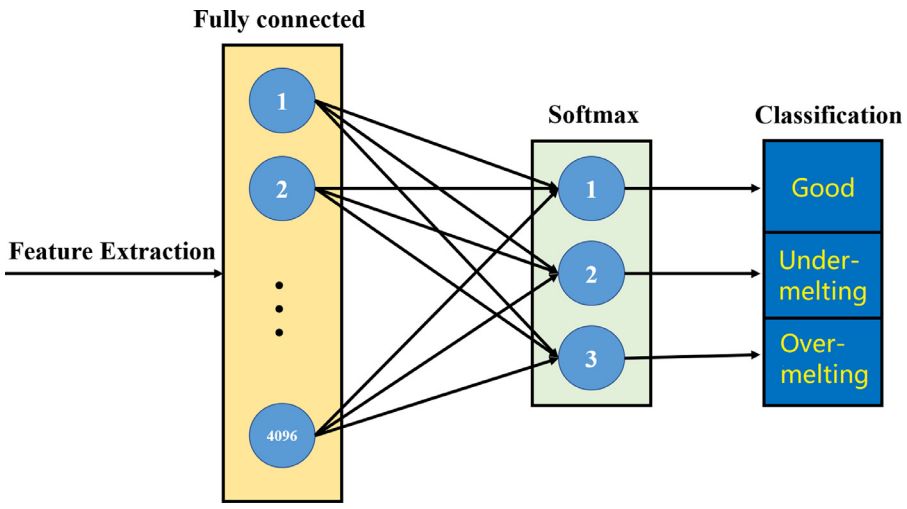

Fig. 10. Fully connected layer with softmax and classification layers.

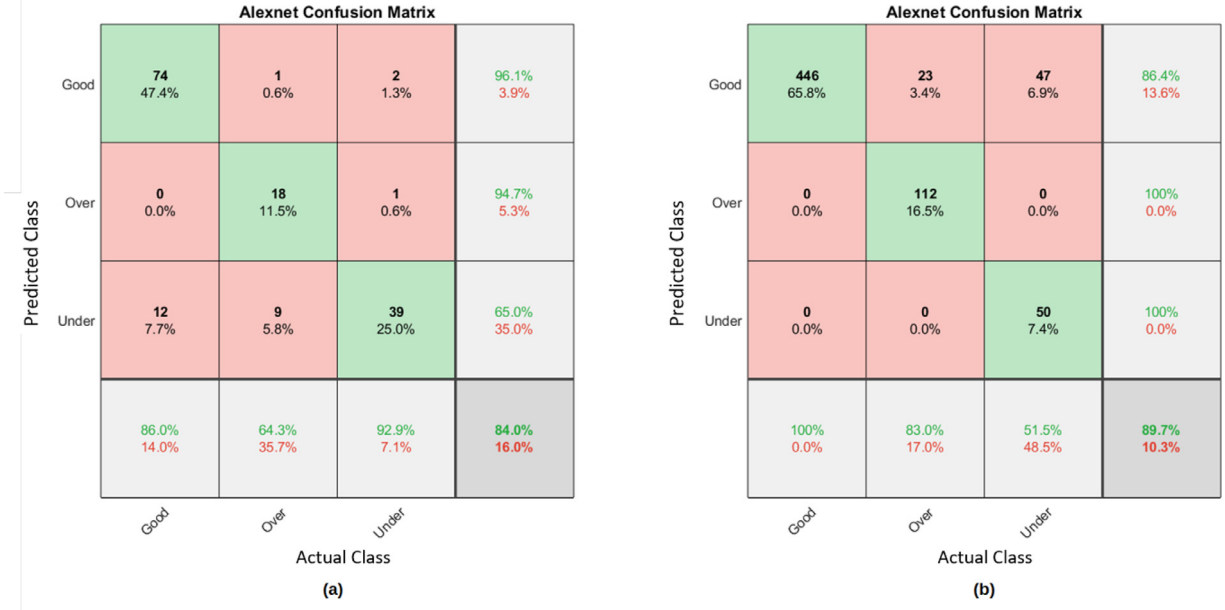

Fig. 11. CNN testing confusion matrices: (a) OT CNN, and (b) melt pool CNN.

horizontally and vertically to represent the actual class and the predicted class, respectively. The first $N \times N$ entries of the confusion matrix show the counts of correct and incorrect classifications. The diagonal entries of the confusion matrix show the amount of correct classifications made by the CNN of each category. The remaining entries show the number of incorrect classifications and the specific types of errors made. The last row summarizes the accuracy given a specific ground-truth class while the last column summarizes the accuracy given a predicted class. Finally, the last (lower-right) entry of the confusion matrix summarizes the overall accuracy. According to the confusion matrix, the melt pool CNN is able to achieve an overall accuracy of 89.7% and the OT CNN achieves an overall accuracy of 84.0%. More specifically, for the OT CNN, 7.7% of the classifications correspond to false-positive reports, in which proper-melting images are classified as over-melting or under-melting. Additionally, 1.9% of the reports are false-negative reports, in which over-melting or under-melting images are classified as proper-melting, and 6.4% of the reports are misidentified errors of disturbances, in which over-melting images are labelled as under-melting or vice versa. For the melt pool CNN, there are no false-positive or misidentified errors for all errors are false-negative reports.

Although both CNNs yield acceptable overall accuracy, we observe that each CNN performs better when categorizing certain types of disturbances. This is due to the different focus on the disturbances by the MPM and OT sensors. The detailed breakdown of the OT and melt pool CNN performances is shown by the confusion matrices (a) and (b) in Fig. 11, respectively. The OT CNN has an accuracy of 92.9% in categorizing under-melting cases while the melt pool CNN has an accuracy of 100% and 83% in categorizing proper-melting and over-melting cases, respectively. Thus, it is desirable to combine the results of both CNNs to fully exploit their respective advantages. Therefore, a cross-validation scheme is formulated to further increase the overall accuracy.

4. Cross-validation utilizing two sensor data analytics

As mentioned in Section 2.4, the OT and MPM sensors have different fields of view. Also, it was demonstrated that the OT CNN performs better at identifying under-melting cases while the

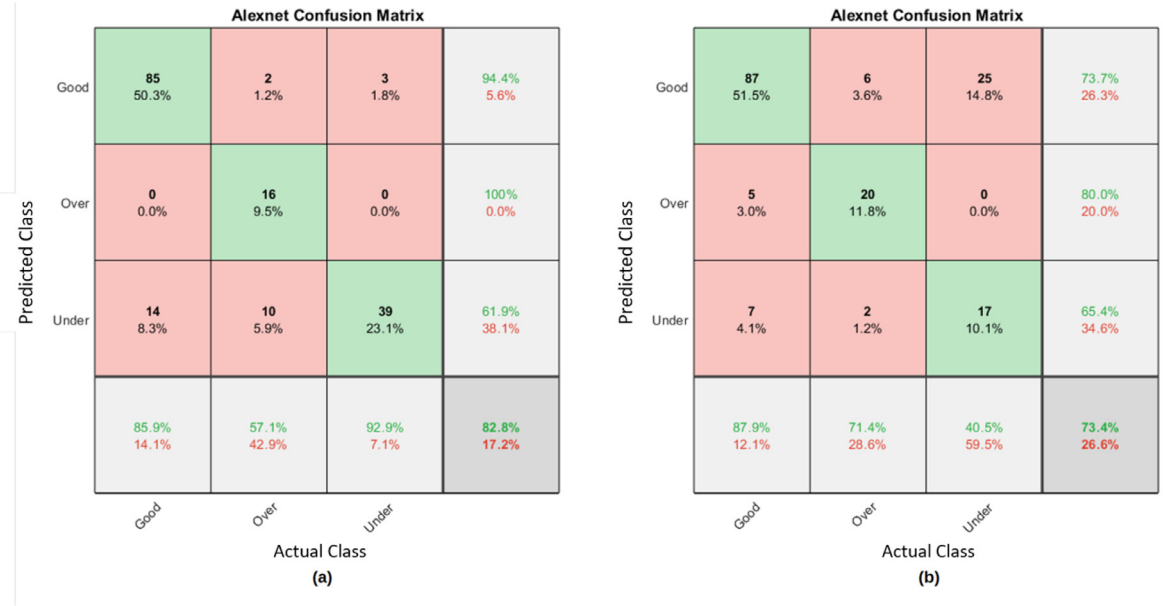

Fig. 12. Confusion matrices of the (a) OT CNN and (b) clustered melt pool CNN classifying the 169 regions of interest.

melt pool CNN performs better at identifying over-melting and proper-melting cases. Therefore, a cross-validation scheme is proposed to combine the respective strength of these two sensors and balance the CNN analytic bias. The framework and results of this cross-validation scheme are discussed in detail in this section.

4.1. Cross-validation scheme formulation

In the cross-validation scheme, we attempt to classify regions of the build part using results from both the melt pool and the OT CNNs. Each region of interest is 0.1 mm $\times$ 0.1 mm in size, which is the same dimension as one regional OT image. First, both the melt pool and the OT CNNs will be used to separately classify each region and assign a confidence level to that classification. Then, if one region is classified differently according to the two CNNs, the confidence levels from both CNNs will be used to cross-validate the classification results and determine a final classification. Additionally, a final equivalent confidence level is provided through meta-analysis.

The location labels are used to correlate the OT and melt pool images with the associated CNN labels. Since the field of view of melt pool images is smaller than each region of interest, one region corresponds to six melt pool images. Therefore, all melt pool images corresponding to the same region are collected and compared to its ground truth. For each melt pool image, a confidence level is provided by the softmax layer, and a confidence level threshold is set to filter out melt pool images with low classification confidence levels. Based on the remaining qualified classifications, an empirically determined criterion is used to decide on the melt pool classification of a region, i.e., disturbances that span over three consecutive melt pool images can be correlated with disturbances on the regional OT images. Therefore, if there exist several potential classifications for a region, this empirical criterion is applied to determine the final classification. Additionally, the combined confidence level of the regional melt pool categorization is the average of the qualified categorizations, which is calculated as follows:

$$\mu = \frac{1}{n}\sum_{i}^{n} x_i \tag{15}$$

where μ is the average confidence, n is the number of qualified classifications, and x_i is the individual confidence level of each associated melt pool image.

After the melt pool CNN results are correlated with each separated region of the build part, we obtain the confidence level of the same region from the OT CNN and compare it with the results from the melt pool CNN. Since the dimensions of each region of interest are the same as the OT regional image's dimensions, the OT CNN classifications and confidence levels do not need to be further processed. Using the confidence levels from both CNNs, a cross-validated final classification is determined to be the higher classification confidence level result between the two CNNs. In addition, the final confidence level can be calculated through the use of inverse-variance weighting, which is a meta-analysis method, to combine the result of different studies on the same problem. It aims to minimize the variance through the calculation of the inverse-variance weighted average, $\hat{x}$, which is calculated as follows:

$$\sigma^2 = \frac{1}{n}\sum_{i}^{n}(x_i - \mu)^2 \tag{16}$$

where n is the number of images, x_i is the individual confience level of each OT or MP image and σ^2 is the variance of either the OT or the melt pool CNN.

$$\hat{x} = \frac{\left(\frac{x_{OT}}{\sigma_{OT}^2}\right) + \left(\frac{x_{MP}}{\sigma_{MP}^2}\right)}{\left(\frac{1}{\sigma_{OT}^2}\right) + \left(\frac{1}{\sigma_{MP}^2}\right)} \tag{17}$$

where $\hat{x}$ is the inverse-variance weighted confidence level and σ^2 is the variance of either the OT or the melt pool CNN.

4.2. Case study

The proposed cross-validation scheme is validated with a case study using images from one layer of the DMLS process generated from the FEM simulation. A total of 1000 melt pool images and 169 OT regional images corresponding to that layer are cross-validated with each other. Individual CNN analysis is first processed and the classification results for the OT sensor analytics are shown in Fig. 12(a). To prepare for the cross-validation scheme, the 1000 melt pool images are first labelled with their respective locations

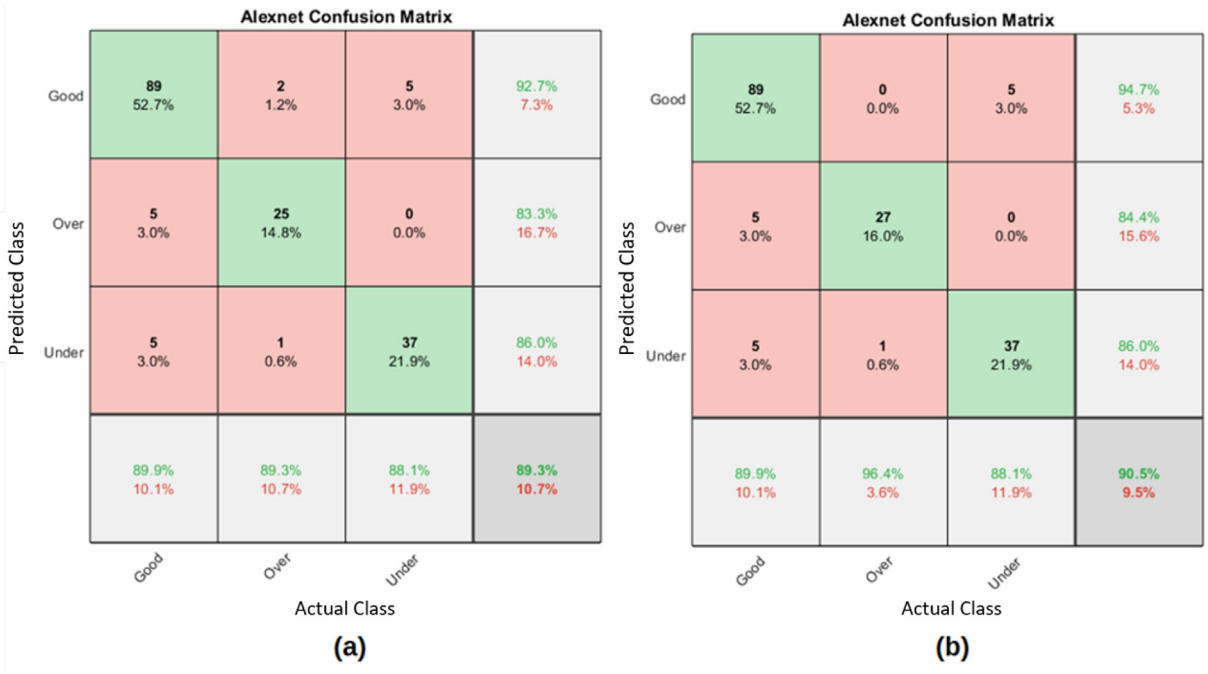

Fig. 13. Confusion matrices showing the accuracy of the cross-validation scheme with confidence thresholds of (a) 72% and (b) 87%. Some rounding errors exist due to summation.

and correlated to each region of interest. These melt pool images are then categorized and given a confidence level using the previously trained melt pool CNN. Next, two confidence level thresholds of 72% and 87% are tested to eliminate unreliable classifications.

Fig. 12(a) shows the detailed breakdown of the OT CNN classifying each region of interest. The overall accuracy of the OT CNN is 82.8% which is similar to the previous testing accuracy. A total of 8.3% of the classifications are false-positive reports, 3% of the reports are false-negative reports, and 5.9% of the reports are misidentified errors of disturbances. Fig. 12(b) displays the testing accuracy of the melt pool CNN categorization for each region of interest. The final accuracy is 73.4% with 7.1% false-positive reports, 18.4% false-negative reports, and 1.2% misidentified errors. While the melt pool CNN overall classifies the regions of interest less accurately than the OT CNN, it makes less misidentified errors than the OT CNN. Specifically, for the classification of over-melting images, the melt pool CNN has an accuracy of 71.4%, which is much higher than the 57.1% in the OT CNN. As a result, we apply a cross-validation decision scheme to improve the overall accuracy of the data analytics process.

Two confidence thresholds of 72% and 87% are tested for the cross-validation and their final decision accuracies are shown in Fig. 13. According to the two cross-validated confusion matrices in Fig. 13, the overall accuracy of the cross-validation is substantially higher than that of the individual, non-cross-validated CNN, shown in Fig. 12. The number of false-positive, false-negative, and misidentified errors all have been reduced, which demonstrates that the cross-validation scheme successfully incorporates the advantages of both sensors. A comparison between all types of errors and the overall accuracies of the individual OT, melt pool and cross-validation methods is shown in Fig. 14. The amount of misidentified errors drops from 5.9% when solely using the OT CNN to 0.6% when cross-validation is performed between the OT CNN and the melt pool CNN. The explanation for this decrease can be related back to the different type of sensor data used. As mentioned in Section 2.4, the MPM and the OT sensors have different fields of view and thus capture different aspects of disturbances. The cross-validation scheme utilizes information from both sensors and therefore is able to detect and classify disturbances more accurately. The amount of false-positive reports also decreases from 8.3% to 6% with the implementation of the cross-validation scheme. This decrease is not as significant as that of the misidentified errors due to the fact that both sensors face a similar performance issue when presented with false-positive errors. The major difference between the 72% and 87% cross-validation threshold scheme is the amount of false-negative reports. By setting a higher confidence threshold, the 87% threshold result is selected to contain more trustworthy classifications than its 72%

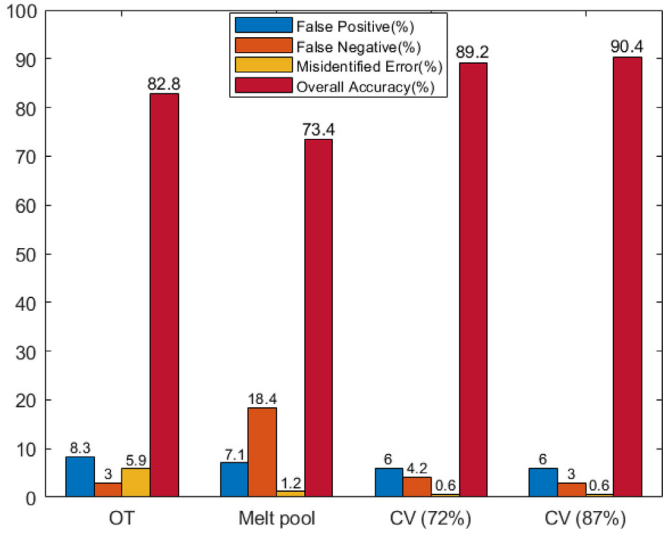

Fig. 14. Bar graph showing the percent of false-positives, false-negatives, misidentified errors, and overall accuracy of all considered methods. (For interpretation of the references to colour in this figure legend, the reader is referred to the web version of this article.)

counterpart and thus resulting in a slight decrease in false-negative reports. At the same time, the 87% threshold results also contain less data than the 72% threshold result as labels with confidence level between 72% and 87% are discarded. This may result in the cross-validation scheme being less robust due to the limited data pool size as more results are discarded when the confidence level threshold is increased. Finally, we assign a final confidence level to each image through the calculation of the inverse-variance weighted average between the OT and MP CNN confidence level. For one correctly identified over-melting image, the OT CNN has a confidence level of 76.3% with a variance of 3.64% and the MP CNN has a confidence level of 89.2% with a variance 0.932%. The final confidence level assigned using the inverse-variance weighted average method is 88.4% For one misidentified over-melting image, the OT CNN has a confidence level of 78.3% with a variance of 3.64% and the MP CNN has a confidence level of 73.2% with a variance of 0.932%. The final confidence level assigned is 73.5%.

5. Conclusion

In this work, an integrated cross-validation framework using CNNs for the in-situ processing of the DMLS process was constructed. First, the DMLS process was simulated using COMSOL Multiphysics, a physics-based simulation software, to obtain the melt pool behavior and layer-wise OT image data through finite element method (FEM) modeling. Specifically, the FEM model described the heat transfer behavior of the DMLS process, accounting for phase change, conduction, convection, and radiation. Then, the FEM model results were validated against both experimental data and analytical solutions. Next, the thermal data from the validated FEM model were processed into two sets of images corresponding to the output format of the two types of realistic sensors: the melt pool monitoring (MPM) sensor and the optical tomography (OT) sensor. Specifically, the temperature contour map at each timestep reproduced the output from the MPM sensor, and the locally averaged temperature history of the build layer reproduced the output of the OT sensor. Afterwards, these two sets of images were labelled and used to train their respective machine learning model for each sensor. A convolutional neural network (CNN) was chosen to be the main machine learning technique used in this work. Transfer learning was performed on the AlexNet CNN backbone for each sensor, and both trained CNNs achieve reasonable testing accuracy individually. A single-layer case study demonstrated that the classification accuracy of identifying OT images using OT CNN alone was 82.8%. To further improve the classification accuracy, a cross-validation scheme was formulated and applied to the model sensor outputs. Based on the statistical analysis of the classification results of the melt pool and the OT CNNs, the cross-validation scheme determined a final label as well as a final confidence level. With the implementation of the cross-validation scheme, the testing accuracy increased up to 90.4% while the amount of misidentified errors decreased by 5.3%. It can be concluded that this cross-validation approach of utilizing CNN for in-situ DMLS process monitoring shows promise as it accurately predicts disturbances and can be potentially applied to real-time manufacturing monitoring platforms. In future works, we will attempt to further localize the disturbance and increase disturbance identification accuracy using more advanced deep learning techniques, such as Region-based CNN (R-CNN).

Declaration of Competing Interest

The authors declare that they have no known competing financial interests or personal relationships that could have appeared to influence the work reported in this paper.

CRediT authorship contribution statement

Yi Ming Ren: Conceptualization, Methodology, Software, Writing - original draft. **Yichi Zhang:** Conceptualization, Methodology, Software, Writing - original draft. **Yangyao Ding:** Conceptualization, Methodology, Software, Writing - original draft. **Yongjian Wang:** Software. **Panagiotis D. Christofides:** Writing - review & editing.

Acknowledgement

Financial support from the Department of Energy is gratefully acknowledged.

References

Amari, S.I., 1993. Backpropagation and stochastic gradient descent method. Neurocomputing 5 (4–5), 185–196.
Arısoy, Y.M., Criales, L.E., Özel, T., 2019. Modeling and simulation of thermal field and solidification in laser powder bed fusion of nickel alloy IN-625. Opt. Laser Technol. 109, 278–292.
Baumers, M., Beltrametti, L., Gasparre, A., Hague, R., 2017. Informing additive manufacturing technology adoption: total cost and the impact of capacity utilisation. Int. J. Prod. Res. 55 (23), 6957–6970.
Clijsters, S., Craeghs, T., Buls, S., Kempen, K., Kruth, J.-P., 2014. In situ quality control of the selective laser melting process using a high-speed, real-time melt pool monitoring system. Int. J. Adv. Manuf. Technol. 75, 1089–1101.
Costa, L., Vilar, R., Reti, T., Deus, A., 2005. Rapid tooling by laser powder deposition: process simulation using finite element analysis. Acta Mater. 53, 3987–3999.
Delgado, J., Ciurana, J., Rodríguez, C.A., 2012. Influence of process parameters on part quality and mechanical properties for DMLS and SLM with iron-based materials. Int. J. Adv. Manuf. Technol. 60, 601–610.
Dong, Z., Liu, Y., Wen, W., Ge, J., Liang, J., 2019. Effect of hatch spacing on melt pool and as-built quality during selective laser melting of stainless steel: modeling and experimental approaches. Materials (Basel) 12, 50.
Everton, S.K., Hirsch, M., Stravroulakis, P., Leach, R.K., Clare, A.T., 2016. Review of in-situ process monitoring and in-situ metrology for metal additive manufacturing. Mater. Des. 95, 431–445.
Frazier, W.E., 2014. Metal additive manufacturing: a review. J. Mater. Eng. Perform. 23, 1917–1928.
Gibson, I., Rosen, D.W., Stucker, B., et al., 2014. Additive Manufacturing Technologies, 17. Springer.
Gong, H., Rafi, K., Gu, H., Starr, T., Stucker, B., 2014. Analysis of defect generation in Ti–6Al–4V parts made using powder bed fusion additive manufacturing processes. Addit. Manuf. 1, 87–98.
Goodfellow, I., Bengio, Y., Courville, A., 2016. Deep Learning. MIT press.
Grünberger, T., Domröse, R., 2014. Optical in-process monitoring of direct metal laser sintering (DMLS): a revolutionary technology meets automated quality inspection. Laser Tech. J. 11, 40–42.
Khurana, J., Hanks, B., Frecker, M., 2018. Design for additive manufacturing of cellular compliant mechanism using thermal history feedback. In: ASME 2018 International Design Engineering Technical Conferences and Computers and Information in Engineering Conference. American Society of Mechanical Engineers Digital Collection.
Krizhevsky, A., Sutskever, I., Hinton, G.E., 2012. Imagenet classification with deep convolutional neural networks. In: Advances in Neural Information Processing Systems, pp. 1097–1105.
Leal, R., Barreiros, F., Alves, L., Romeiro, F., Vasco, J., Santos, M., Marto, C., 2017. Additive manufacturing tooling for the automotive industry. Int. J. Adv. Manuf. Technol. 92, 1671–1676.
Liu, R., Wang, Z., Sparks, T., Liou, F., Newkirk, J., 2017. Aerospace applications of laser additive manufacturing. In: Laser Additive Manufacturing. Elsevier, pp. 351–371.
Ma, C., Vadali, M., Duffie, N.A., Pfefferkorn, F.E., Li, X., 2013. Melt pool flow and surface evolution during pulsed laser micro polishing of Ti_6Al_4V. J. Manuf. Sci. Eng. 135 (6).
Mohr, G., Altenburg, S.J., Ulbricht, A., Heinrich, P., Baum, D., Maierhofer, C., Hilgenberg, K., 2020. In-situ defect detection in laser powder bed fusion by using thermography and optical tomography comparison to computed tomography. Metals (Basel) 10, 103.
Nandwana, P., Peter, W.H., Dehoff, R.R., Lowe, L.E., Kirka, M.M., Medina, F., Babu, S.S., 2016. Recyclability study on Inconel 718 and Ti-6Al-4V powders for use in electron beam melting. Metallurgic. Mater. Trans. B 47, 754–762.
Peralta, A., Enright, M., Megahed, M., Gong, J., Roybal, M., Craig, J., 2016. Towards rapid qualification of powder-bed laser additively manufactured parts. Integrat. Mater. Manuf. Innovat. 5, 154–176.
Ramos, D., Belblidia, F., Sienz, J., 2019. New scanning strategy to reduce warpage in additive manufacturing. Addit. Manuf. 28, 554–564.
Romano, J., Ladani, L., Sadowski, M., 2016. Laser additive melting and solidification of Inconel 718: finite element simulation and experiment. JOM 68 (3), 967–977.
Rosenthal, D., 1941. Mathematical theory of heat distribution during welding and cutting. Weld. J. 20, 220–234.

Sadowski, M., Ladani, L., Brindley, W., Romano, J., 2016. Optimizing quality of additively manufactured inconel 718 using powder bed laser melting process. Addit. Manuf. 11, 60–70.

Scime, L., Beuth, J., 2019. Using machine learning to identify in-situ melt pool signatures indicative of flaw formation in a laser powder bed fusion additive manufacturing process. Addit. Manuf. 25, 151–165.

Scott, C., 2017. EOS introduces EOSTATE Exposure OT, First Commercial Optical Tomography System for Additive Manufacturing. https://3dprint.com/178624/eos-eostate-exposure-ot/ (Accessed on 2020-07-19).

Singh, S., Ramakrishna, S., 2017. Biomedical applications of additive manufacturing: present and future. Curr. Opin. Biomed. Eng. 2, 105–115.

Tang, M., Pistorius, P.C., Beuth, J.L., 2017. Prediction of lack-of-fusion porosity for powder bed fusion. Addit. Manuf. 14, 39–48.

Yan, W., Lian, Y., Yu, C., Kafka, O.L., Liu, Z., Liu, W.K., Wagner, G.J., 2018. An integrated process–structure–property modeling framework for additive manufacturing. Comput Method. Appl. Mech. Eng. 339, 184–204.

Yuan, B., Giera, B., Guss, G., Matthews, I., Mcmains, S., 2019. Semi-supervised convolutional neural networks for in-situ video monitoring of selective laser melting. In: Proceedings of Winter Conference on Applications of Computer Vision (WACV). IEEE, Waikoloa Village, Hawaii, pp. 744–753.

Zhang, Y., Hong, G.S., Ye, D., Zhu, K., Fuh, J.Y., 2018. Extraction and evaluation of melt pool, plume and spatter information for powder-bed fusion AM process monitoring. Mater. Des. 156, 458–469.

EOS, 2018. EOSTATE MeltPool: Real-time process monitoring for EOS M 290. https://www.eos.info/software/monitoring-software/meltpool-monitoring (Accessed on 2020-07-19).